JGR Space Physics

RESEARCH ARTICLE
10.1029/2024JA033039

Key Points:

- An algorithm has been developed to identify geomagnetic disturbances in 10 s magnetometer data
- Geomagnetic disturbances occur mainly in two populations, pre-midnight, on region 1 upward field-aligned currents (FACs) and dawn on the boundary
- The latitude that the geomagnetic disturbances occur at is dependent on the FAC boundary

Correspondence to:
G. E. Bower,
geb23@leicester.ac.uk

Citation:
Bower, G. E., Imber, S., Milan, S. E., Schillings, A., Fleetham, A. L., & Gjerloev, J. W. (2024). Location of geomagnetic disturbances in relation to the field aligned current boundary. *Journal of Geophysical Research: Space Physics*, *129*, e2024JA033039. https://doi.org/10.1029/2024JA033039

Received 10 JUL 2024
Accepted 22 SEP 2024

Location of Geomagnetic Disturbances in Relation to the Field Aligned Current Boundary

G. E. Bower[1], S. Imber[1], S. E. Milan[1], A. Schillings[1,2], A. L. Fleetham[1], and J. W. Gjerloev[3]

[1]School of Physics and Astronomy, University of Leicester, Leicester, UK, [2]Department of Physics, Umeå University, Umeå, Sweden, [3]Johns Hopkins University Applied Physics Laboratory, Laurel, MD, USA

Abstract Geomagnetic disturbances (GMDs) are rapid fluctuations in the strength and direction of the magnetic field near the surface of the Earth which can cause electric currents to be induced in the ground. The geomagnetically induced currents (GICs) can cause damage to pipelines and power grids. A detection algorithm has been developed to identify rapid changes in 10 s averaged magnetometer data. This higher resolution data is important in capturing the most rapid changes associated with extreme GIC events. The algorithm has been used on an array of ground-based magnetometers from SuperMAG data from 2010 to 2022, creating a new list of global GMDs. Data from the Active Magnetosphere and Planetary Electrodynamics Response Experiment (AMPERE) is used to place the observed GMDs in the context of the global pattern of magnetosphere-ionosphere field-aligned currents (FACs). A dawn sector population of GMDs is found to lie near the boundary between the region 1 and region 2 FACs, while a pre-midnight sector population is found to occur poleward of the FAC boundary on region 1 upward FACs. It is also shown that the latitude of the GMDs expands with the FAC boundary and their occurrence peaks around 77° magnetic latitude.

Plain Language Summary Rapid changes called geomagnetic disturbances (GMDs) in the Earth magnetic field can lead to currents flowing at the surface of the Earth. When these currents flow through infrastructure such as power grids and pipeline, damage can occur which can lead to a loss of services and impact society. It therefore important to understand the conditions necessary for these current to form. The rapid changes can be measured by ground magnetometers. A newly developed algorithm that uses 10 s data from 2010 to 2022, from SuperMAG magnetometers around the globe, has been developed. The GMDs are then places in context to the field aligned currents (FACs) measure by the Active Magnetosphere and Planetary Electrodynamics Response Experiment (AMPERE) that flow in the magnetosphere. A population that is found to occur at dawn lies equatorward of the FAC boundary. A population of GMDs found to occur at pre-midnight lie poleward of the FAC boundary. The latitude that the GMDs occur at is dependent on the FAC boundary.

1. Introduction

During space weather events, geomagnetically induced currents (GICs) have been observed at the surface of the Earth. These currents were first reported to have an impact on a hydro power transformer in 1989 (Boteler et al., 1989) and have since been known to be able to cause damage to other infrastructure such as pipelines and power grids (Albertson et al., 1973; Campbell, 1978; Marshall et al., 2010). GICs are not typically measured directly but are observed via ground-based magnetometers that measure the associated geomagnetic disturbance (GMD) in one or more components (Pulkkinen et al., 2008; Rogers et al., 2021; Viljanen, 1997), where a GMD is a large change in $d\mathbf{B}/dt$, which is the rate of change of the geomagnetic field. Large $d\mathbf{B}/dt$ associated with GMDs have been called "spikes" (Schillings et al., 2022). Extreme GMDs are of particular interest, as these are most likely to cause impacts on society through damage or disruption of key infrastructures. Molinski et al. (2000) describe severe events as having a 300 nT change in the magnetic field in 1 min. Many factors determine if a GMD will cause a GIC that is harmful, such as ground conductance, the direction, relative to the disturbance, of pipelines and power grids (Grawe et al., 2018; Pulkkinen et al., 2008) but understanding where and when rapid GMDs occur and their drivers is an important step.

Previous studies typically have focused on the global impact (Pirjola, 2000; Schillings et al., 2022) or on regional impacts (Freeman et al., 2019; Ngwira et al., 2018; Orr et al., 2021; Zou et al., 2022) of sudden perturbations in the Earth's magnetic field linked to phenomena such as storms, substorms and aurora. These are periods of high geomagnetic activity that can cause intensification of the currents flowing in the ionosphere, which can lead to GMDs.

Regional studies had identified "hotspots" in magnetic local time for the occurrence of GMDs in the pre-midnight sector and the pre-noon/dawn sector. Weigel et al. (2002) used 30-min average intervals of data from the IMAGE magnetometer network between 1998 and 1999 to identify the large pre-midnight population of large $d\mathbf{B}/dt$ and a smaller pre-noon population. Juusola et al. (2015) used 10 s magnetometer data from the IMAGE network over a 20 year period between 1994 and 2013 and confirmed the existence of both populations. The IMAGE network has a small spatial extent but the "hotspots" of GMDs have been confirmed to occur globally during storm times by Schillings et al. (2022). Schillings et al. (2022) used 1 min SuperMAG data to globally investigate $d\mathbf{B}/dt$ during 307 magnetic storms between 1980 and 2020 in the north-south (N) and east-west (E) direction. They also showed that "spikes" initially occur in the pre-midnight sector but as a storm progresses they develop in time toward the morning sector.

The pre-midnight population has been suggested to be associated with substorm activity due to the electrojets and the formation of the substorm current wedge (Juusola et al., 2015; Schillings et al., 2022; Weigel et al., 2002). Weigel et al. (2002) identified that the pre-noon population occurs at the transition regions between the eastward and westward electrojets. Weigel et al. (2003) went on to suggest that this was due to ULF pulsations linked to Kelvin-Helmholtz activity on the dawn flank of the magnetosphere. Alternately omega bands have been suggested as the cause of the dawn population (Juusola et al., 2015; Schillings et al., 2022). Omega bands are an auroral wave-like feature that drift eastward and can occur in the morning sector (Opgenoorth et al., 1983). However Zou et al. (2022) used THEMIS all-sky imagers alongside THEMIS and Geophysical Institute Magnetometer Array magnetometers to investigate large $d\mathbf{B}/dt$ during storms between 2015 and 2016 and found that many auroral drivers, such as poleward expanding auroral bulges, auroral streamers, poleward boundary intensifications, omega bands, pulsating auroras can all lead to large $d\mathbf{B}/dt$. Pc5 waves have also been suggested as a possible cause for the dawn population of GMDs (Ngwira et al., 2018).

Milan et al. (2023) looked at the global occurrence of $d\mathbf{B}/dt$ using 1-min SuperMAG magnetometer data over solar cycles 23 and 24. They found three local time hotspots, a pre-midnight region, a dawn sector region and a pre-noon sector region, which they suggested were associated with substorm onset, omega bands and KHI respectively.

Previous studies have indicated the need for higher resolution magnetometer data (Schillings et al., 2022) to detect and fully understand the effects of short-lived GMDs, as the most rapid changes are associated with extreme GICs. A spike that occurs over a few seconds is smoothed out in 1 min cadence data leading to the calculated $d\mathbf{B}/dt$ being smaller than in reality, thus a higher temporal resolution is needed. Without this, the ability to predict the occurrence of potentially dangerous GMDs is limited.

This study has developed a detection algorithm to identify rapid changes in 10 s averaged magnetometer data, making use of the available higher resolution SuperMAG data. SuperMAG has stations that record data at 1 s cadence, but we smooth this to 10 s to remove the impact of erroneous readings that are present in the 1 s data. We also place the GMDs in the context of the global field-aligned current (FAC) systems using AMPERE data.

2. Algorithm

A detection algorithm has been developed to identify rapid changes in the magnetic field measured by magnetometers. The algorithm was developed using SuperMAG data from 17 to 19 March 2015. These dates were chosen as they cover the St Patrick's day storm in 2015, during which many GMDs occurred (Carter et al., 2016; Schillings et al., 2023). The SuperMAG data is provided in the N, E, Z coordinate system. Where N is the local magnetic North-South direction with positive northward, E is the local magnetic East- West direction with positive eastward and Z is the vertical direction with positive downwards.

The algorithm first calculates a 10 s average of the 1 s SuperMAG data in each direction separately. The difference between consecutive magnetic field measurements in each component direction is then calculated. If the difference between consecutive magnetic field measurements is greater than a set spike threshold, T, a possible geomagnetic disturbance (GMD) is identified. For this study T is set at 50 nT/10 s. The list of possible geomagnetic disturbance GMDs is then assessed to remove erroneous events. In order to do this, four threshold values are calculated. Figure 1 show schematics of how each threshold works.

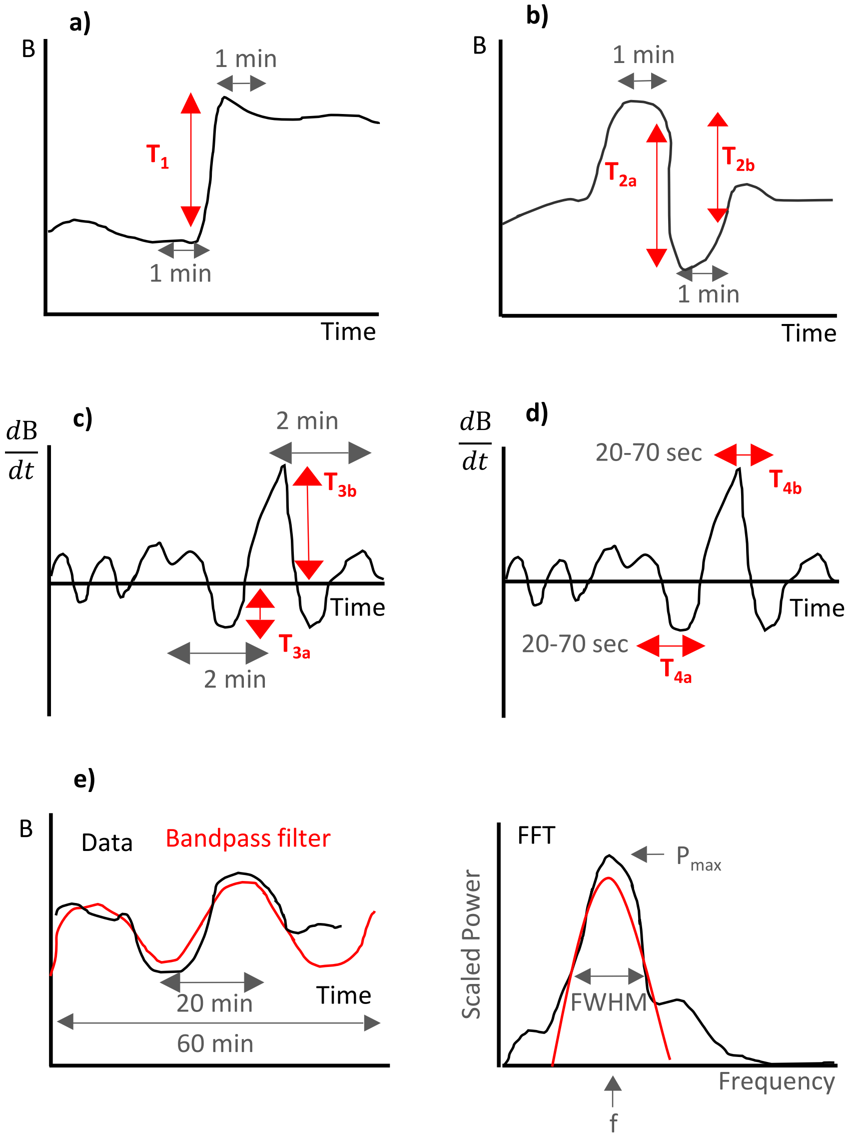

Figure 1. Schematic showing each threshold used in the detection algorithm. (a) T_1, (b) T_2, (c) T_3, (d) T_4, and (e) wave related values.

- The first threshold, T_1, (Figure 1a) is the difference between the median values of the magnetometer data in the minute before and after the potential GMD. A GMD is considered bad if T_1 is less than 80% of the spike threshold. T_1 is used to remove non-physical spikes that return to near original conditions in 1 min.
- The second threshold, T_2, looks at the minute before and after to see how rapidly the magnetic field has been varying. See Figure 1b. A GMD is considered bad if either value is less than 40% of the spike threshold.

The next two thresholds look at the rate of change of the magnetic field using the $d\mathbf{B}/dt$ values.

- Threshold 3, T_3, (Figure 1c) assesses if there has been a spike of greater than the spike threshold magnitude in the opposite direction in the 2 min before or after the potential GMD. If either T_3 value is $1.5T$ then the potential GMD is considered doubtful.
- T_4 looks at the mean $d\mathbf{B}/dt$ of the 20–70 s before and after the GMD to see if the magnetic field is varying or not (Figure 1d). If the absolute value of T_4 either before or after the GMD is less than 5.0 nT/10 s then the GMD is considered doubtful. This threshold removes spikes that occur too close to a data gap to be confident in the measurement.

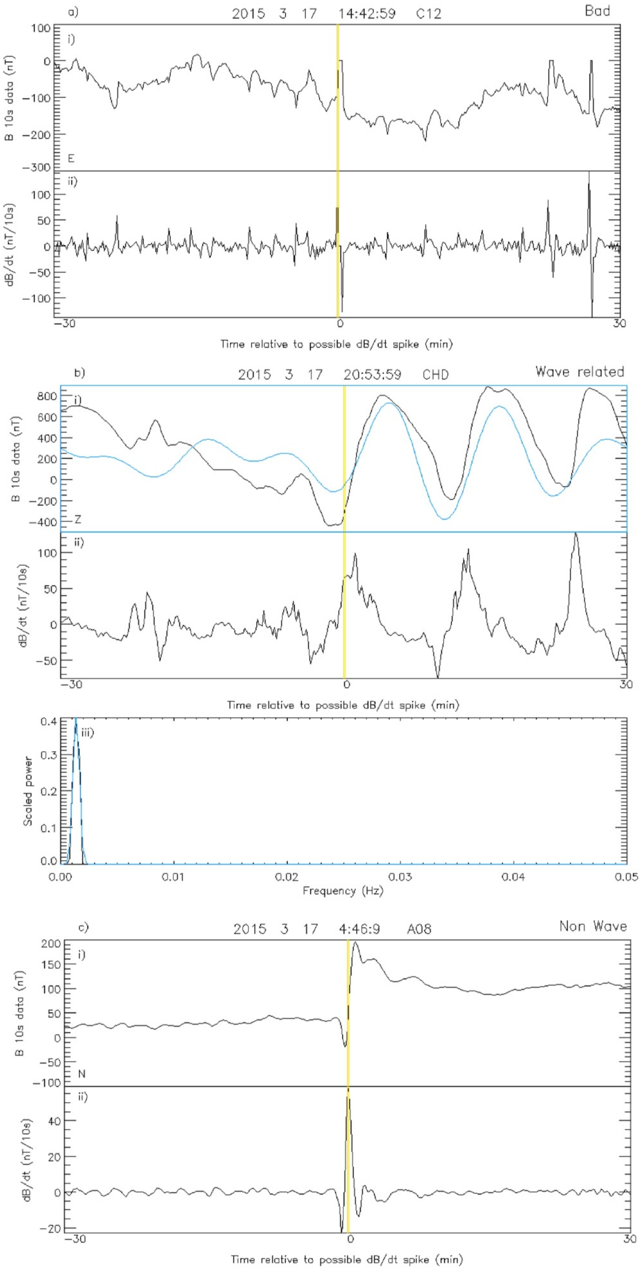

Figure 2. Example GMD detections and their classification. Each panel shows an hour of magnetometer data from a particular coordinate direction centered on the potential GMD indicated by the vertical yellow line. The classification is in the top right of each panel. The title of each panel shows that date and time along with the stations ID. The magnetic field direction of the data is in the lower left hand corner. Panels (a and c) consists of two sub panels where (i) is the magnetometer data and (ii) is the $d\mathbf{B}/dt$ data. Panel (b) has a further third sub panel (iii) showing the FFT of the fitted data in black and the Gaussian fit in blue. Top sub panel of panel (b) also contains the bandpass filter in blue.

Any GMDs identified by the algorithm are then further assessed to see if they are related to wave activity. This is done to help determine the cause of the GMDs. The GMDs are assessed via a bandpass filter performed on the hour of magnetometer data centered on the GMD (Figure 2). The bandpass filter limits are varied between $\frac{1}{900}$ Hz and $\frac{1}{40}$ Hz to find the best fit based on a cross correlation with the data (CC). A smaller 20 min bandpass filter is also applied (CC_2). An FFT (fast Fourier transform) is then performed on the filtered data providing the maximum power $P_{\max}$ in fractional power spectral density and related frequency (Figure 1e left). A GMD is considered to be related to a wave if $P_{\max}$ is greater than 0.02, the frequency is above approximately 0.001 Hz and one of the four following conditions applies

- The difference between the two cross correlations ($CC_2 - CC$) is less than 0.34 and CC_2 is greater than 0.69.
- $CC_2 - CC$ is less than 0.4 and CC_2 is greater than 0.85
- $CC_2 - CC$ is less than 0.5 and CC_2 is greater than 0.89
- $P_{\max}$ is greater than 0.35 and CC_2 is greater than 0.7 and CC is greater than 0.5.

For each GMD that is determined to be related to a wave, the frequency is recorded along with an estimate of the error based on the FWHM of a Gaussian fitted to the peak of the FFT (Figure 1e right red curve). All threshold used were found by trail and error.

Figure 2 shows examples of GMD in SuperMAG data, with the magnetometer data and the $d\mathbf{B}/dt$ data. A third panel with the FFT for the wave related GMD is also included. Panel a shows a bad GMD that is removed from the data set. This is flagged as bad because it fails the T_2 criteria. Panel b shows a wave related GMD and panel c shows a non wave related GMD. It is important to note that each 10 s is considered as a separate GMD even if multiple occur in succession.

During the time period used to develop the algorithm, 17–19 March 2015, 3,033 potential GMDs were found. Table 1 shows the classification of the potential GMDs from both the algorithm and by eye for this period. The by eye classification was found from visual inspection of all 3,033 potential GMDs. From this it can be seen that the algorithm has an effectiveness of 76.9% correctly classifying potential GMDs. The algorithm also has a false positive detection rate of 4.9% and a false negative detection rate of 13.9%.

3. Results

Analysis was carried out on SuperMAG one second data from 2010 to 2022. The SuperMAG data used has been pre-processed using the SuperMAG analysis technique (Gjerloev, 2012) and is in the N, E, Z coordinate system. 448,104 potential GMDs were identified by the algorithm which have an amplitude of greater than 50 nT over 10 s, in agreement with the methods of Milan et al. (2023). 103,984 non-wave and 46,220 wave related GMDs were found, 143,111 of which were in the northern hemisphere because the coverage of magnetometer is greater in the northern hemisphere. The majority of GMDs are in the N direction (64,872) with 37,998 in the Z direction and 47,334 in the E direction.

Figure 3 shows the breakdown of how many GMDs occur by month and by year in the top panels, in which the black line shows the non-wave GMDs and the red the wave related GMDs. The y-axis is expressed as a percentage of the number of non-wave and wave related GMDs respectively, so that comparisons between the two groups is clearer. The numbers of non-wave and wave related GMDs peak around the equinoxes, in March and September

Table 1
Algorithm Effectiveness

		Algorithm			
		Good	Wave	Bad	Total
Eye	Good	684	136	46	866
	Wave	113	676	239	1,028
	Bad	9	26	971	1,006
	Total	806	838	1,256	

Note. Comparison of classification of GMD from 17 to 19 March 2015 by eye and by the algorithm.

(Figure 3a), These peaks correspond to variations in overall geomagnetic activity, as indicated by the distribution of storms and substorms (Freeman et al., 2019; Kataoka & Pulkkinen, 2008). As shown in Figure 3c based on the SOPHIE substorm list (Forsyth et al., 2015) between 2010 and 2022 the number of substorms peaked in March and then in September and October with a minimum in June. The number of storms between 2010 and 2020 also has two peaks around the equinoxes one in September and one in March–April from the Walach and Grocott (2019) storm list Figure 3e.

The occurrence of substorms and storms is also able to explain the yearly variability. Figure 3b shows the number of GMDs by year which peaks in 2017 but is variable over the solar cycle. 2012 and 2015 had particularly large storms (Walach & Grocott, 2019) and an increase in the number of GMDs detected is also seen in these years as expected. 2014 has fewer substorms and fewer GMDs are detected in that year. Hamrin et al. (2023) found that GMDs occur during the declining phase of the solar cycle and related it to the high solar wind velocity. The distribution in Figure 3b is similar to the one found by Milan et al. (2023) where they also show that GMDs occur more frequently during the declining phase of the solar cycle. The results shown here include the start of solar cycle 25 and the number of GMDs can be seen to be increasing again after a minimum in 2020.

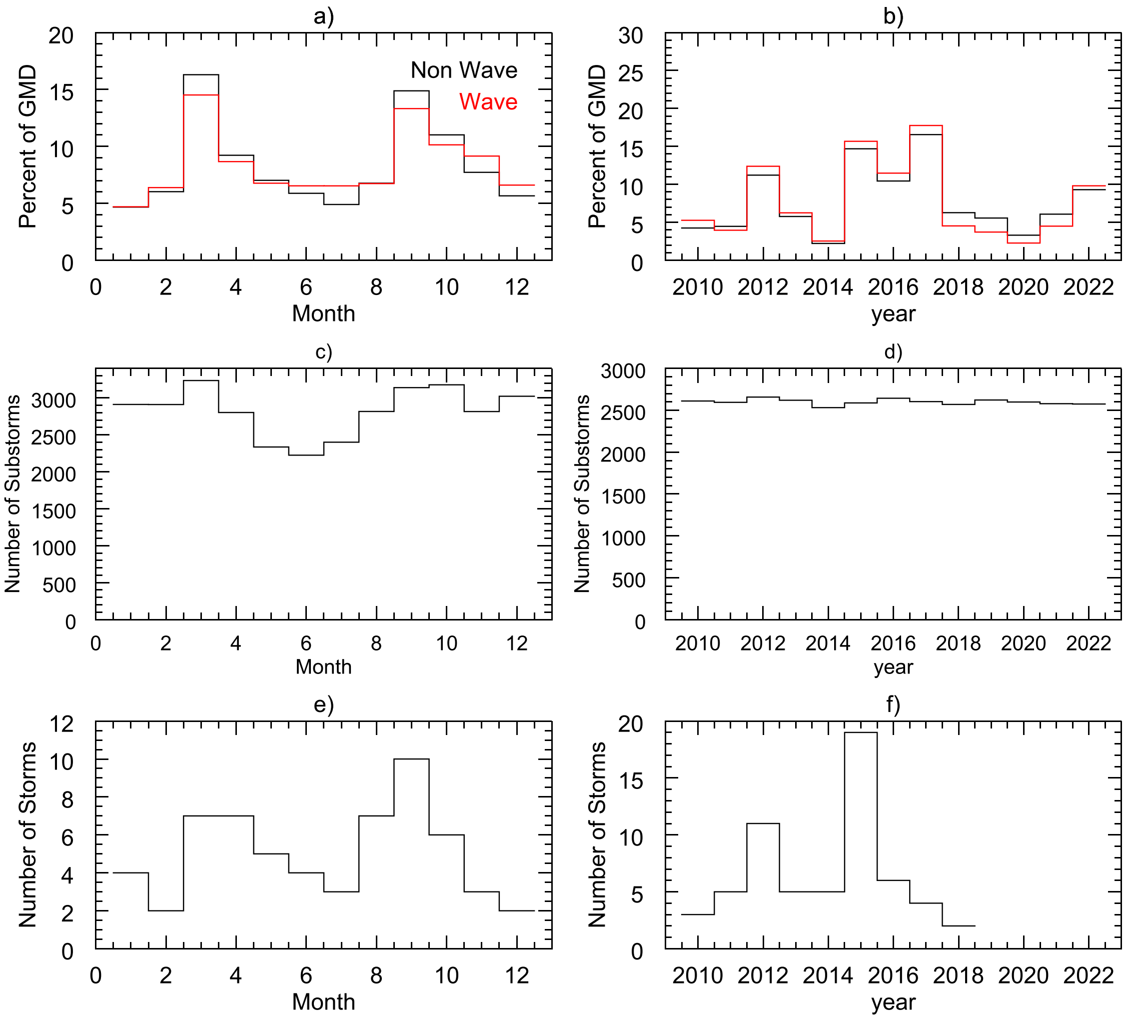

Figure 3. Histograms of distribution of GMD by (a) month and (b) year. Black line is non wave GMD and red line is wave related GMD. (c and d) Number of substorms by month and year using SOPHIE (80 ept) substorm list (Forsyth et al., 2015). (e and f) Number of storms by month and year using Walach and Grocott (2019) list.

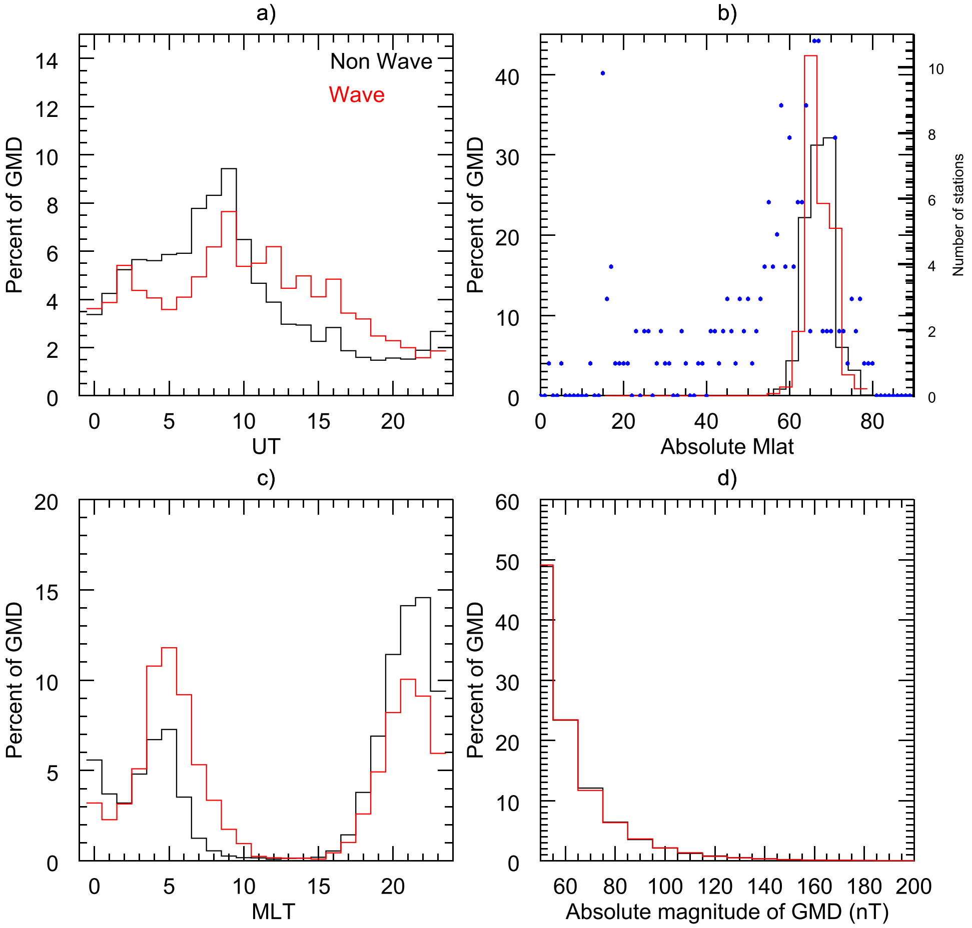

Figure 4. Histograms of distribution of GMD by (a) UT, (b) magnetic latitude, (c) magnetic local time, and (d) absolute magnitude of GMD. Black line is non wave GMD and Red line is wave related GMD.

Figure 4 shows the breakdown of how many GMDs occur by universal time (UT), absolute magnetic latitude (mLat), magnetic local time (MLT) and absolute magnitude of the GMDs. As in Figure 3 the black line shows the non-wave GMDs and the red the wave related GMDs. The peak of the UT distributions for both categories is co-located at 9 UT but the non wave related GMDs are skewed to earlier UT than the wave related GMDs that has a larger spread (Figure 4a). This is discussed further below.

In Figure 4b the blue circles indicate the number of stations, with data that were available at each degree of latitude. The number of non-wave GMDs peaks at around 70° and at around 65° for wave related GMDs.

The MLT distributions (Figure 4c) show two clear populations of GMDs, one at dawn and one pre-midnight. These are the two previously identified "hot spots" of GMDs (Schillings et al., 2022) which are identified again in this higher resolution data set. The non-wave GMDs occur more often in the pre-midnight sector whereas the wave related GMDs occur more often at dawn (Figure 4c). The smaller population of non wave GMD at dawn are increased in number by the miss classified wave related GMD. This was verified using the 17–19 March time period used to test the algorithm. All the wave related GMDs are found to have similar frequencies extracted from the FFT on the bandpass filtered data, with a median value 1.9 ± 2.0 mHz. The error is calculated from the standard deviation of the Gaussian fits to the peak value in the FFT. This places the waves in the ULF range.

Figure 4d shows the distribution of the absolute magnitude of the GMDs; as expected most occur with smaller magnitudes with the distribution trailing off at higher magnitudes following an approximately 1/3 power law and no visible difference between the two groups of GMDs, this is expected at the magnitude of wave or non wave related GMDs is not expected to be different.

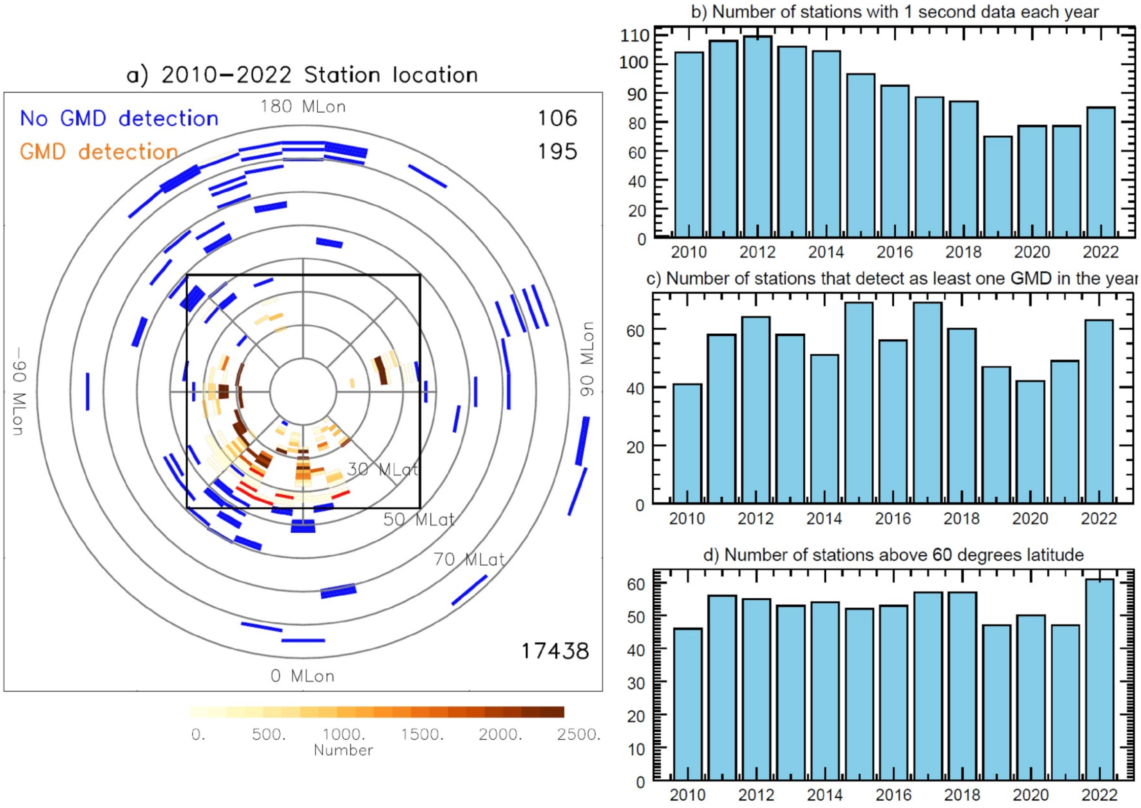

Figure 5. (a) All stations with data between 2010 and 2022 location in magnetic latitude/magnetic longitude plot. The concentric circles are separated by 10° latitude. The blue stations are ones where data was available but no good or wave GMD were identified. The other stations are on a color scale with the darker orange stations having the most GMD detected. (b) Number of stations with available 1 s data each year globally. (c) Number of stations that detect GMD each year globally. (d) Number of stations with available 1 s data above 60° latitude each year.

Figure 5a shows the locations of all the stations with data between 2010 and 2022. The plot is in magnetic longitude with 0 at the bottom and magnetic latitude from 90 at the center to 0 at the outer edge. Both northern hemisphere and southern hemisphere stations are plotted on the same panel. The concentric circles are separated by 10° latitude. The blue stations indicate where data was available but no GMDs were identified between 2010 and 2022. The other stations are on a color scale, with the darker orange stations having the most GMDs detected. From this it can be seen that the majority of the GMDs detections are from stations located at similar latitudes closer to the pole. The square box indicates the area used in the MLT/MLat plots used in Figure 6.

The right hand panels of Figure 5 show how the number of stations varies between years. Figure 5b shows the number of stations per year globally. Figure 5c shows the number of stations that detect GMDs each year globally and Figure 5d shows the number of stations above 60° latitude. Together these panels show that although the number of stations with 1 s data decreases over the time period the number of high latitude stations, that are more likely to detect a GMD, is similar between all the years investigated with a range of between approximately 45 and 60 stations each year.

The UT distributions (Figure 4a) are explained by the spread of magnetometer stations with available 1 s data. As shown in Figure 5a the majority of the high latitude stations that detect GMDs are located in a 135° geomagnetic longitude wide sector. The group of stations passes through the pre-midnight sector at around 3–9 UT thus leading to an increase in the number of GMDs detected at this UT. The same is then true for the wave GMDs as the number peak at around 11–15 UT when the stations pass through the dawn sector. Another factor in this is that not all the stations have available data at all times. We have shown in Figure 5d that the number of stations in the region most likely to detect GMDs, above 60° latitude, is relatively constant even though the number of stations with available data decreases overall (Figure 5b). Above 60° is chosen as from Figure 4c it can be seen that even

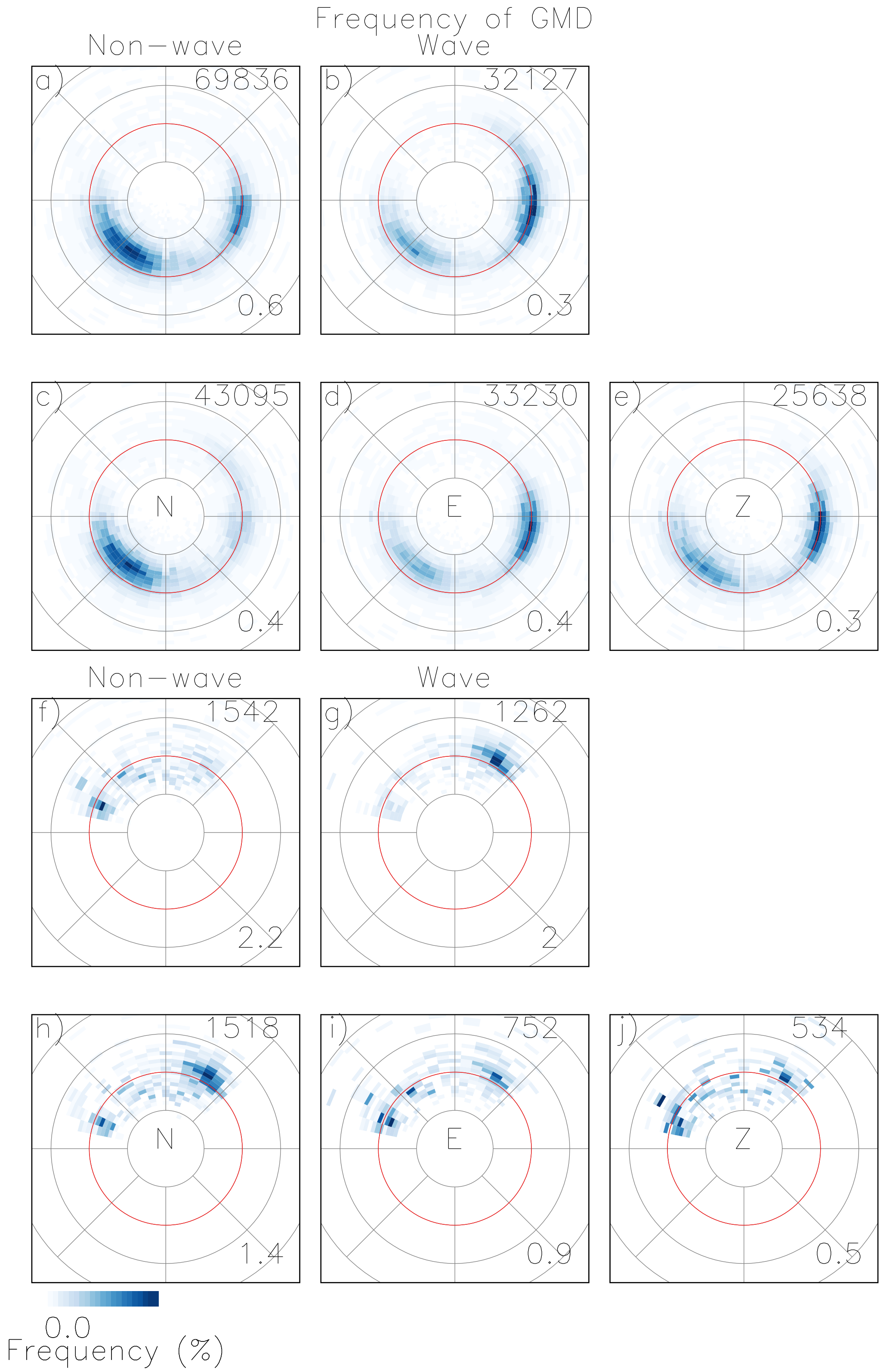

Figure 6. GMD frequency maps scaled to the boundary between the field-aligned currents (FACs). Frequency as a percent of the number of GMD in each group. The maximum percent is given in the lower right hand corner and this is the darkest color on the color scale. The number in the top right show the number of GMD included in the plot. The red circle shows the location of the FAC boundary. The top row first panel is non-wave GMD and the second panel is wave related GMD. The second row is the coordinate directions N, E, Z. The bottom two rows shows only GMDs between 9 and 17 UT in the same layout as the top two rows.

though there are stations with available data large GMD occur most frequently between approximately 60 and 80° absolute magnetic latitude.

We want to investigate the relationship between the location of GMDs and the R1/R2 FAC system (Iijima & Potemra, 1976). It is known that the FACs latitude change with geomagnetic activity (Clausen et al., 2012). To account for these motions, we investigate the location of GMDs relative to the MLT and MLat coordinate system. In Figure 6 the location of the GMDs has been scaled to the FAC boundary, Rb, found from the Active Magnetosphere and Planetary Electrodynamics Response Experiment (AMPERE) data by Milan et al. (2015). The Milan et al. (2015) method works by finding the zero point crossing between the region 1 and region 2 FACs from the AMPERE data maps and fitting a circle to these points. In case of the GMDs the nearest AMPERE map fit is used as AMPERE provides maps every 2 min and that GMD is only included in Figure 6 if the quality threshold of the AMPERE fit is above 0.15 (Milan et al., 2015). 20° colatitude has been chosen as the scaled FAC boundary indicated in red in Figure 6. This coordinate has been referred to as Birkeland Current Boundary (BBC) coordinates (Coxon et al., 2023) and means that poleward of 20° colatitude are the region 1 FAC and equatorward are the region 2 FACs.

From Figure 6 it can be seen that the GMDs in the pre-midnight population sit inside the FAC boundary, co-located with the region 1 upwards FACs. The dawn population lie on the boundary between the region 1 and region 2 FAC. This is the case for both the non-wave and wave related GMDs (Figures 6a and 6b), however the non wave GMDs have a larger pre-midnight population and smaller dawn population compared to the wave related GMDs.

The second row of Figure 6 shows the GMDs split by magnetic field direction. The majority of N direction GMDs occur in the pre-midnight sector where the E and Z direction GMDs occur mainly in the dawn sector. This suggests that the E and Z direction GMDs are dominated by wave related GMDs which also occur primarily near dawn.

The third row of Figure 6 shows the dayside populations with a clear per-noon population in the wave related GMDs that sits outside the FAC boundary. The bottom row of Figure 6 show the dayside GMDs split by magnetic field direction. The pre-noon population is primarily N direction GMDs.

Figure 7a show the distributions of the location of the FAC boundary from the AMPERE current maps, with black showing the background distribution for the period of interest and the red during GMD times. From this it is clear that the GMDs occur when the polar cap is expanded, peaking at around 72° latitude for the background and 67-68° latitude for the GMD times.

The magnitudes of the GMDs is investigated in Figures 7b–7d. The GMDs are split into the MLT populations day, dawn and pre-midnight. The GMDs are then plotted based on their magnitudes and the difference between the absolute latitude of the station that detects a GMD and the location of the associated AMPERE FAC boundary from Milan et al. (2015). As the FAC boundaries from Milan et al. (2015) are circles for which the center point is defined offset from zero degrees colatitude, the GMD locations have to corrected such that they are aligned with the same center. In Figures 7b–7d detections inside the FAC boundary are positive where detections outside the FAC boundary are negative. The color scale shows the number of GMDs in each 10 nT by 1° latitude bin on a log scale. As shown in Figure 4d higher magnitude GMDs are rarer.

The day GMDs have a peak at approximately 130 nT with a slight offset inside the FAC boundary, slight positive values, suggesting that the highest magnitude day GMDs occur just inside of the FAC boundary. As seen from Figure 6f this is a non-wave related population of GMDs. The more distributed pre-noon population of wave related GMDs occur outside the FAC boundary (Figure 6g). The group of GMDs that occur around 15° outside the FAC boundary (Figure 7b) therefore may be related to wave activity. The dawn population peaks at approximately 190 nT at around 1–3° inside the FAC boundary. Finally the pre-midnight population has the highest peak at 230 nT and the largest offset of approximately 4° inside the FAC boundary. This suggests that the highest magnitude GMDs occur within a few degrees of latitude of the FAC boundary. Thus having accurate models for the prediction of the FAC boundary will improve forecast ability of GMDs.

The final panel of Figure 7 shows a frequency map for the magnetic latitude that GMDs are detected for each FAC boundary. From this it can be seen that as the FAC boundary expands to lower latitudes the GMDs are then detected at lower latitudes. This is as expected as during active times, when GMDs are more likely to occur, the

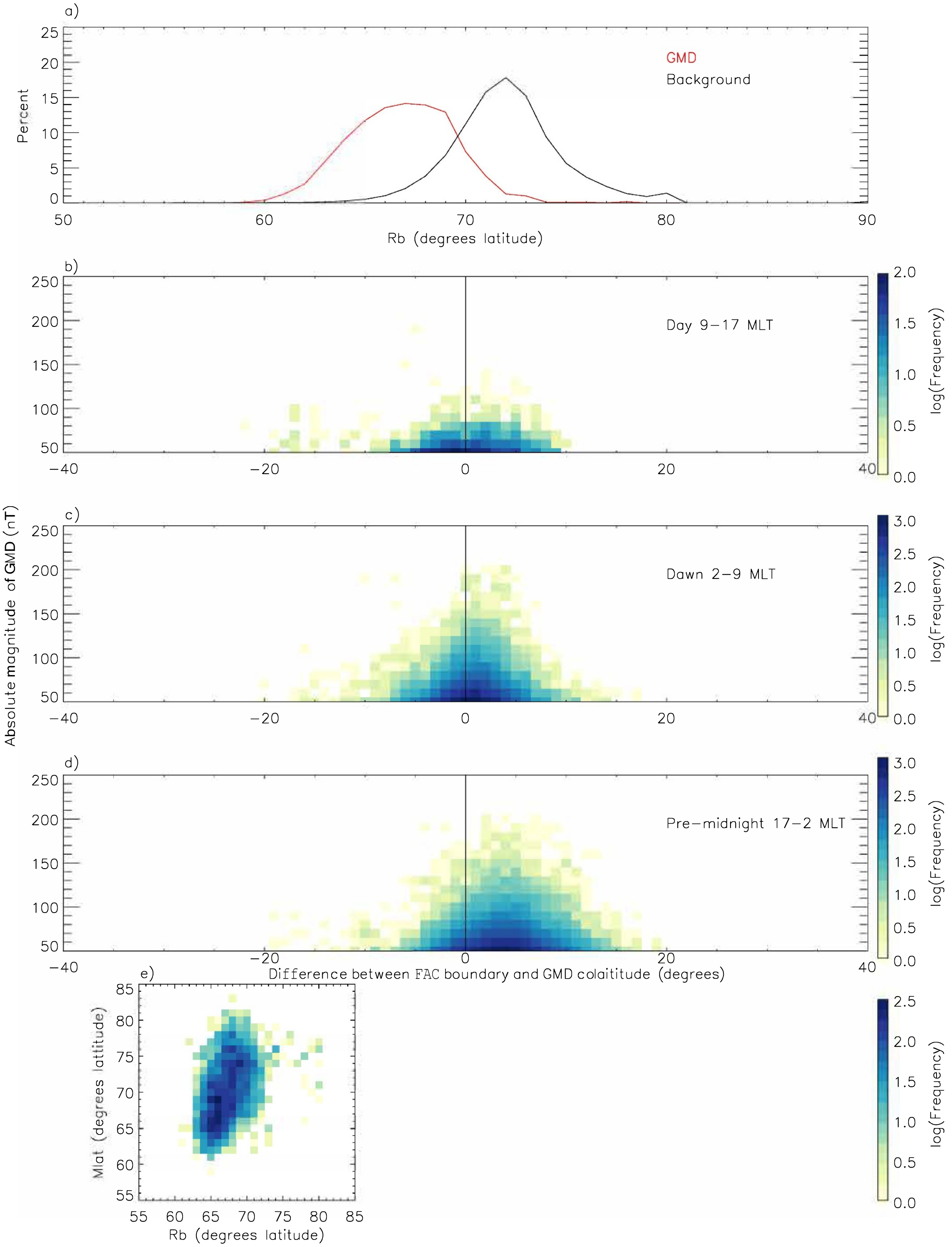

Figure 7. (a) Field-aligned current (FAC) boundary distributions (red) Number of GMD (black) background. (b–d) The difference between the GMD location and the location of the FAC boundary against the absolute magnitude of the GMD. (b) Day, (c) Dawn, (d) Pre-midnight. The red line is a Gaussian fit to the highest 10 magnitude in 1° bins. (e) Frequency map of the magnetic latitude of GMD detections against FAC boundary at time of GMD detection.

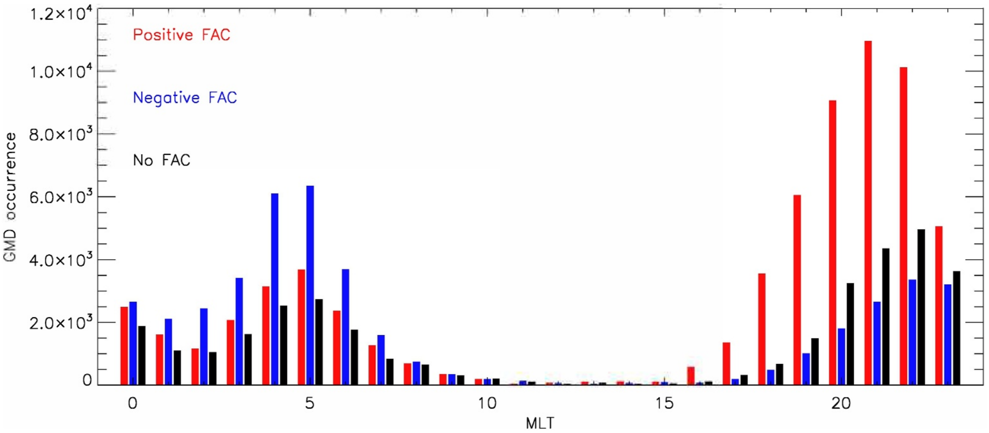

Figure 8. Barplot of GMD at each MLT that are associated with co-located positive field-aligned current (FAC) (red), negative FAC (blue), and no FAC (black).

IMF is southward thus dayside, low latitude reconnection creates more open flux moving the FAC boundary to lower latitudes.

The FAC current associated with GMDs are further investigated in Figure 8. The current magnitude is taken from the nearest AMPERE measurement to the GMD observation. Figure 8 shows the number of GMDs in each MLT bin that are associated with co-located positive FAC (red), negative FAC (blue) and no FAC (black) where no FAC is defined as being between −0.1 and 0.1 μA. Any GMDs that occur during AMPERE data gaps (7,094 GMDs) are removed from Figure 8.

Finally the OMNI solar wind data is investigated at the time of the GMDs. As the OMNI data use is at 1 min resolution (King & Papitashvili, 2005) the value is taken from the minute closest to the time of the GMD. Figure 9 is split into three columns, the GMDs that occur during the day, those near dawn and those that occur around pre-midnight as in Figure 7. The rows are the different OMNI parameters investigated IMF B_z, AL, SymH, solar wind density (Nsw) and solar wind speed (Vsw) respectively. The black lines on each plot are the GMD data where the red line is the background using all available OMNI data between 2010 and 2022.

There is little deviation from the background IMF for both B_x and B_y across the populations (not shown). The dawn and pre-midnight GMDs occur when IMF B_z is more negative (southward), with the dawn population having a wider distribution that extends to more negative values peaking at around −10 nT. The day population is less dependent on the IMF with only a slight preference for southward IMF with the main peak being similar to the background. All three populations occur when the AL index and SymH index have more negative values than the background. The solar wind density is enhanced for the day and dawn populations. The solar wind speed is typically higher for the GMDs, particularly the day population which peaks at around 700 km s^{-1}.

4. Discussion

Geomagnetic disturbances (GMDs) have been identified in 10 s averaged SuperMAG data. Two main populations have been identified, one at dawn and one pre-midnight. These populations are in agreement with those found by previous studies (Juusola et al., 2015; Milan et al., 2023; Schillings et al., 2022; Weigel et al., 2002). The pre-midnight population is dominated by non-wave related GMDs whereas the dawn population is dominated by wave-related GMDs (Figures 6a and 6b). Both populations peak in the equinoxes which is when substorms and storms occur most frequently. This is expected as GMDs are related to periods of active conditions. GMDs also occur predominately in the years when substorm and storms occur most frequently. The number of GMDs peaks during the declining phase of the solar cycle as shown by Milan et al. (2023). A minimum number of GMDs is reached in 2020 during the solar minimum before increasing again.

The GMDs are shown to move equatorward with the FAC boundary (Figure 7e) and the highest amplitude GMDs occur poleward of the FAC boundary within 5° latitude. This suggests that the location of the GMDs is linked to the polar cap boundary.

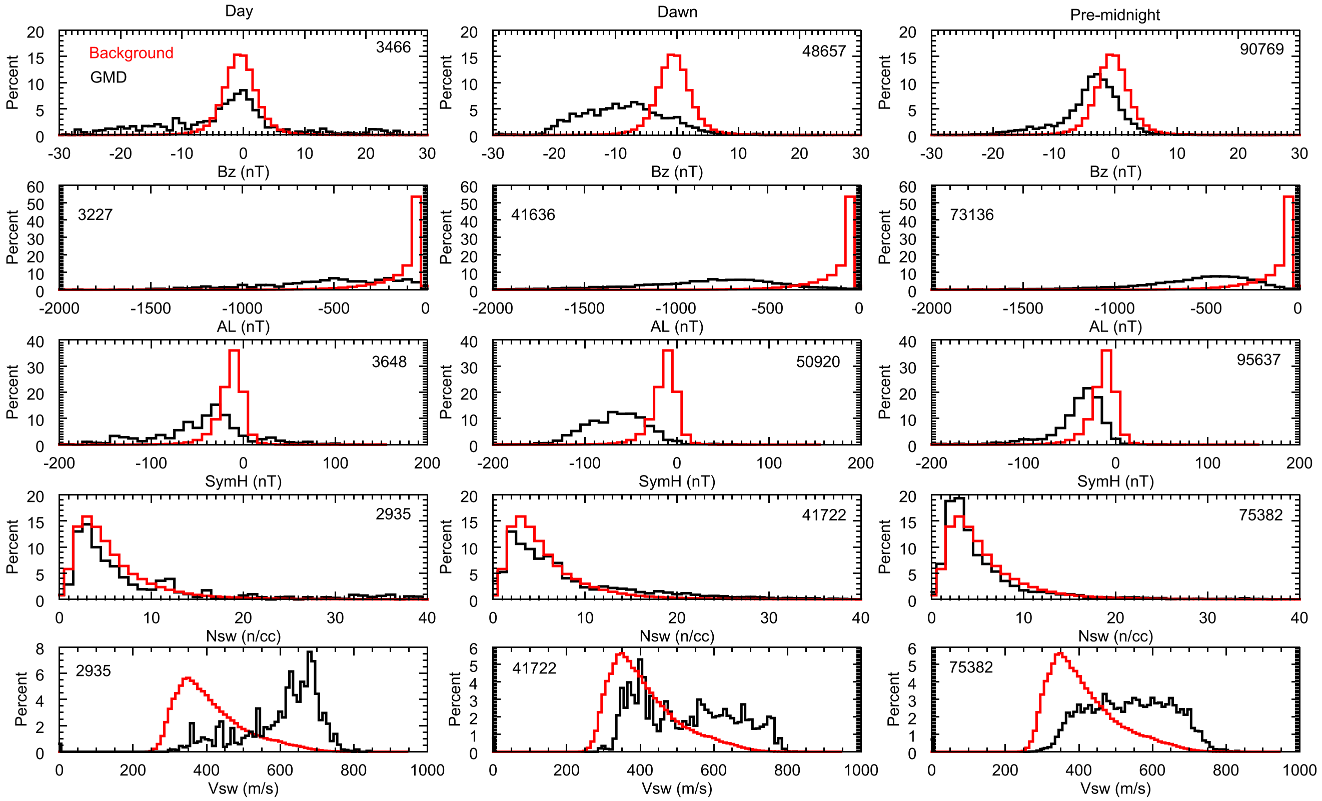

Figure 9. OMNI parameters by row B_z, AL, SymH, Nsw, and Vsw respectively. Columns are MLT of GMD investigated Day, Dawn, and Pre-midnight. The red line is the background OMNI data. The black line is the data closest to the time of the GMD.

The location of the pre-midnight GMDs co-located with the upward region 1 currents (Figures 6 and 8) can be explained, as this population is thought to be linked to substorm activity. The substorm current wedge forms due to sudden enhancements in the westward electrojet leading to enhanced FACs and magnetic perturbations. The regions of upward current is where the most precipitation occurs due to the downward traveling electrons producing rapid changes in ionospheric conductivity.

The dawn population of GMDs is more often co-located with a downward FAC, however it must be noted that the temporal resolution of AMPERE is not as good as the SuperMAG observations. The OMNI data for the dawn GMDs shows that they occur during more intense storms when SymH and B_z are more negative. The dawn population has previously been suggest to be related to omega bands (Juusola et al., 2015; Schillings et al., 2022), Pc5 waves (Ngwira et al., 2018) or auroral streamers during periods of varying AL (Milan et al., 2024). Either explanation can also be applied to the result shown here.

Fleetham et al. (2024) also looked at the FAC current co-located with the GMDs during 5 storm periods: they also found that the pre-midnight sector GMDs occur more frequently on upward FACs and the dawn sector GMDs more frequent for downward current.

The day population in Figures 6f–6j consists of the lowest number of GMDs. It occurs when the solar wind speed is high and the density is also high and is less dependent on the IMF B_z (Figure 9). This dependence on high speed and density could be linked to a pressure pulse or the Kelvin-Helmholtz instability operating on the magnetopause. Of the 3,648 dayside GMDs detected there are an even split of GMDs and wave related GMDs (1818 and 1830 respectively) of which 1542 and 1262 are plotted in Figures 6f and 6g as there is AMPERE Data available to scale to the FAC boundary. The pre-noon population (Figure 6g) has previously been noted by Milan et al. (2023) in 1 min data. They also found it occurs for fast solar wind and near zero B_z due to this they suggest they are related to Kelvin-Helmholtz activity on the dawn flank of the magnetosphere. Our results would support this as the pre-noon population is found in the wave related GMDs. Other authors such as Weigel et al. (2003) have also used Kelvin-

Helmholtz instability to explain GMDs in the pre-noon sector. KHI is thought to operate equally on both flanks of the magnetosphere therefore further work is needed to understand why only a pre-noon population is clearly seen.

Fleetham et al. (2024) has shown that a noon population of GMDs is present during a storm on the 22 June 2015 that occurs after a pressure pulse. They link the GMDs to the compression of the magnetopause due to the pressure pulse and the resulting increase in the magnetopause current. We suggest therefore that the non-wave GMD could be related to pressure pulses where the wave related are likely due to Kelvin-Helmholtz instability with equal probability for each mechanism.

5. Conclusion

An automated detection algorithm has been developed to identify geomagnetic disturbances (GMDs) in ground magnetometer data at 10 s resolution, and these are separated into non wave, and wave-related GMDs. Using the algorithm on SuperMAG data between 2010 and 2022, GMDs with magnitudes over 50 nT are investigated. 10,3984 good GMDs and 46,220 wave-related GMDs were detected. After fitting the location of the GMDs to the FAC (FAC) boundary, a pre-midnight population is found to lie poleward of the FAC boundary on the upward region 1 FAC. The dawn population lies on the boundary of both upward and downward FACs. Investigation of the OMNI data at the times nearest to the GMDs shows that the dawn population occurs during highly negative SymH and B_z and is therefore related to storm times. The pre-midnight population is related to substorm activity as previously suggested. A smaller dayside population occurs during high solar wind speed and higher solar wind density, suggestive of a solar wind pressure pulse generation mechanism or the Kelvin-Helmholtz instability.

Data Availability Statement

The 1-s cadence ("high fidelity") SuperMAG data were obtained from NASA GSFC through the SuperMAG portal at https://supermag.jhuapl.edu/mag/?fidelity=high. The high resolution (1-min) OMNI data used in this study were obtained from the NASA Goddard Space Flight Center (GSFC) Space Physics Data Facility OMNIWeb portal at https://omniweb.gsfc.nasa.gov/form/om_filt_min.html. The AMPERE current map data used by Milan et al. (2015) to determine the FAC boundary used in this study can be obtained from https://ampere.jhuapl.edu/download/. The FAC radius data can be accessed via https://doi.org/10.25392/leicester.data.11294861.v1 (Milan, 2019). The SOPHIE substorm list is an extension of the list for (Forsyth et al., 2015) where the supporting information provides data from 1996 to 2014 at https://agupubs.onlinelibrary.wiley.com/action/downloadSupplement?doi=10.1002%2F2015JA021343&file=jgra52264-sup-0003-supinfo.txt provided by C. Forsyth. The Walach and Grocott (2019) storm list was accessed from https://doi.org/10.5281/zenodo.4922994. The GMD list created using the algorithm described and used in this paper is published at https://doi.org/10.25392/leicester.data.26954074.v1.

Acknowledgments

GEB, SMI and SEM were supported by the Natural Environment Research Council (NERC), UK, Grant NE/W006766/1. AS was supported by Vetenskapråde, Swedish Research Council, Grant VR 2021-06683. ALF was supported by STFC studentship. For the purpose of open access, the author has applied a Creative Commons Attribution (CC BY) license to the Author Accepted Manuscript version arising from this submission. We would like to thank C. Forsyth for providing the extended SOPHIE substorm list between 2010 and 2022. We acknowledge use of NASA/GSFC's Space Physics Data Facility's CDAWeb service (at http://cdaweb.gsfc.nasa.gov) and OMNI data. For the ground magnetometer data we gratefully acknowledge: INTERMAGNET, Alan Thomson; CARISMA, PI Ian Mann; CANMOS, Geomagnetism Unit of the Geological Survey of Canada; The S-RAMP Database, PI K. Yumoto and Dr. K. Shiokawa; The SPIDR database; AARI, PI Oleg Troshichev; The MACCS program, PI M. Engebretson; GIMA; MEASURE, UCLA IGPP and Florida Institute of Technology; SAMBA, PI Eftyhia Zesta; 210 Chain, PI K. Yumoto; SAMNET, PI Farideh Honary; IMAGE, PI Liisa Juusola; Finnish Meteorological Institute, PI Liisa Juusola; Sodankylä Geophysical Observatory, PI Tero Raita; UiT the Arctic University of Norway, Tromsø Geophysical Observatory, PI Magnar G. Johnsen; GFZ German Research Centre For Geosciences, PI Jürgen Matzka; Institute of Geophysics, Polish Academy of Sciences, PI Anne Neska and Jan Reda; Polar Geophysical Institute, PI Alexander Yahnin and Yarolav Sakharov; Geological Survey of Sweden, PI Gerhard Schwarz; Swedish Institute of Space Physics, PI Masatoshi Yamauchi; AUTUMN, PI Martin Connors; DTU Space, Thom Edwards and PI Anna Willer; South Pole and McMurdo Magnetometer, PI's Louis J. Lanzarotti and Alan T. Weatherwax; ICESTAR; RAPIDMAG; British Artarctic Survey; McMac, PI Dr. Peter Chi; BGS, PI Dr. Susan Macmillan; Pushkov Institute of Terrestrial Magnetism, Ionosphere and Radio Wave Propagation (IZMIRAN); MFGI, PI B. Heilig; Institute of Geophysics, Polish Academy of Sciences, PI Anne Neska and Jan Reda; University of L'Aquila, PI M. Vellante; BCMT, V. Lesur and A. Chambodut; Data obtained in cooperation with Geoscience Australia, PI Andrew Lewis; AALPIP, co-PIs Bob Clauer and Michael Hartinger; MagStar, PI Jennifer Gannon; SuperMAG, PI Jesper W. Gjerloev; Data obtained in cooperation with the Australian Bureau of Meteorology, PI Richard Marshall. References to the AMPERE technique can be found in Milan et al. (2015). We gratefully acknowledge the use of AMPERE data provided by JHU/APL, PIs Brian Anderson/Sarah Vines. This analysis uses the newly-processed AMPERE data.

References

Albertson, V., Thorson, J. M., Clayton, R. E., & Tripathy, S. C. (1973). Solar-induced-currents in power systems: Cause and effects. *IEEE Transactions on Power Apparatus and Systems*, *2*, 471–477. https://doi.org/10.1109/TPAS.1973.293746

Boteler, D., Shier, R., Watanabe, T., & Horita, R. (1989). Effects of geomagnetically induced currents in the BC Hydro 500 kV system. *IEEE Transactions on Power Delivery*, *4*(1), 818–823. https://doi.org/10.1109/61.19275

Campbell, W. H. (1978). Induction of auroral zone electric currents within the Alaska pipeline. *Pure and Applied Geophysics*, *116*(6), 1143–1173. https://doi.org/10.1007/BF00874677

Carter, B., Yizengaw, E., Pradipta, R., Weygand, J., Piersanti, M., Pulkkinen, A., et al. (2016). Geomagnetically induced currents around the world during the 17 March 2015 storm. *Journal of Geophysical Research: Space Physics*, *121*(10), 10–496. https://doi.org/10.1002/2016JA023344

Clausen, L., Baker, J., Ruohoniemi, J., Milan, S. E., & Anderson, B. (2012). Dynamics of the region 1 Birkeland current oval derived from the Active Magnetosphere and Planetary Electrodynamics Response Experiment (AMPERE). *Journal of Geophysical Research*, *117*(A6), A06233. https://doi.org/10.1029/2012JA017666

Coxon, J. C., Chisham, G., Freeman, M. P., Forsyth, C., Walach, M.-T., Murphy, K. R., et al. (2023). Extreme Birkeland currents are more likely during geomagnetic storms on the dayside of the Earth. *Journal of Geophysical Research: Space Physics*, *128*(12), e2023JA031946. https://doi.org/10.1029/2023ja031946

Fleetham, A. L., Milan, S. E., Imber, S. M., Bower, G. E., Gjerloev, J. W., & Vines, S. K. (2024). The relationship between large dB/dt and field-aligned currents during five geomagnetic storms. *Journal of Geophysical Research: Space Physics*, *129*(7), e2024JA032483. https://doi.org/10.1029/2024JA032483

Forsyth, C., Rae, I., Coxon, J., Freeman, M., Jackman, C., Gjerloev, J., & Fazakerley, A. (2015). A new technique for determining Substorm Onsets and Phases from Indices of the Electrojet (SOPHIE). *Journal of Geophysical Research: Space Physics*, *120*(12), 10–592. https://doi.org/10.1002/2015JA021343

Freeman, M. P., Forsyth, C., & Rae, I. J. (2019). The influence of substorms on extreme rates of change of the surface horizontal magnetic field in the United Kingdom. *Space Weather*, *17*(6), 827–844. https://doi.org/10.1029/2018SW002148

Gjerloev, J. (2012). The SuperMAG data processing technique. *Journal of Geophysical Research*, *117*(A9), A09213. https://doi.org/10.1029/2012JA017683

Grawe, M. A., Makela, J. J., Butala, M. D., & Kamalabadi, F. (2018). The impact of magnetic field temporal sampling on modeled surface electric fields. *Space Weather*, *16*(11), 1721–1739. https://doi.org/10.1029/2018SW001896

Hamrin, M., Schillings, A., Opgenoorth, H., Nesbit-Östman, S., Krämer, E., Araújo, J., et al. (2023). Space weather disturbances in non-stormy times: Occurrence of dB/dt spikes during three solar cycles. *Journal of Geophysical Research: Space Physics*, *128*(10), e2023JA031804. https://doi.org/10.1029/2023JA031804

Iijima, T., & Potemra, T. A. (1976). The amplitude distribution of field-aligned currents at northern high latitudes observed by TRIAD. *Journal of Geophysical Research*, *81*(13), 2165–2174. https://doi.org/10.1029/JA081i013p02165

Juusola, L., Viljanen, A., Van De Kamp, M., Tanskanen, E., Vanhamäki, H., Partamies, N., & Kauristie, K. (2015). High-latitude ionospheric equivalent currents during strong space storms: Regional perspective. *Space Weather*, *13*(1), 49–60. https://doi.org/10.1002/2014SW001139

Kataoka, R., & Pulkkinen, A. (2008). Geomagnetically induced currents during intense storms driven by coronal mass ejections and corotating interacting regions. *Journal of Geophysical Research*, *113*(A3), A03S12. https://doi.org/10.1029/2007JA012487

King, J., & Papitashvili, N. (2005). Solar wind spatial scales in and comparisons of hourly Wind and ACE plasma and magnetic field data. *Journal of Geophysical Research*, *110*(A2), A02104. https://doi.org/10.1029/2004JA010649

Marshall, R., Waters, C., & Sciffer, M. (2010). Spectral analysis of pipe-to-soil potentials with variations of the Earth's magnetic field in the Australian region. *Space Weather*, *8*(5), S05002. https://doi.org/10.1029/2009SW000553

Milan, S. E. (2019). AMPERE R1/R2 FAC radii [Dataset]. *Figshare*. https://doi.org/10.25392/leicester.data.11294861.v1

Milan, S. E., Bower, G. E., Fleetham, A. L., Imber, S. M., Schillings, A., Opgenoorth, H., et al. (2024). Occurrence and causes of large *dB*/*dt* events and AL bays in the pre-midnight and dawn sectors. *Journal of Geophysical Research: Space Physics*, *129*(10), e2024JA032811. https://doi.org/10.1029/2024JA032811

Milan, S. E., Carter, J. A., Korth, H., & Anderson, B. J. (2015). Principal component analysis of Birkeland currents determined by the Active Magnetosphere and Planetary Electrodynamics Response Experiment. *Journal of Geophysical Research: Space Physics*, *120*(12), 10–415. https://doi.org/10.1002/2015JA021680

Milan, S. E., Imber, S. M., Fleetham, A. L., & Gjerloev, J. (2023). Solar cycle and solar wind dependence of the occurrence of large dB/dt events at high latitudes. *Journal of Geophysical Research: Space Physics*, *128*(4), e2022JA030953. https://doi.org/10.1029/2022JA030953

Molinski, T., Feero, W., & Damsky, B. (2000). Shielding grids from solar storms [power system protection]. *IEEE Spectrum*, *37*(11), 55–60. https://doi.org/10.1109/6.880955

Ngwira, C. M., Sibeck, D., Silveira, M. V., Georgiou, M., Weygand, J. M., Nishimura, Y., & Hampton, D. (2018). A study of intense local dB/dt variations during two geomagnetic storms. *Space Weather*, *16*(6), 676–693. https://doi.org/10.1029/2018SW001911

Opgenoorth, H., Oksman, J., Kaila, K., Nielsen, E., & Baumjohann, W. (1983). Characteristics of eastward drifting omega bands in the morning sector of the auroral oval. *Journal of Geophysical Research*, *88*(A11), 9171–9185. https://doi.org/10.1029/JA088iA11p09171

Orr, L., Chapman, S., & Beggan, C. (2021). Wavelet and network analysis of magnetic field variation and geomagnetically induced currents during large storms. *Space Weather*, *19*(9), e2021SW002772. https://doi.org/10.1029/2021SW002772

Pirjola, R. (2000). Geomagnetically induced currents during magnetic storms. *IEEE Transactions on Plasma Science*, *28*(6), 1867–1873. https://doi.org/10.1109/27.902215

Pulkkinen, A., Pirjola, R., & Viljanen, A. (2008). Statistics of extreme geomagnetically induced current events. *Space Weather*, *6*(7), S07001. https://doi.org/10.1029/2008SW000388

Rogers, N. C., Wild, J. A., Eastoe, E., & Huebert, J. (2021). Climatological statistics of extreme geomagnetic fluctuations with periods from 1 s to 60 min. *Space Weather*, *19*(11), e2021SW002824. https://doi.org/10.1029/2021SW002824

Schillings, A., Palin, L., Bower, G. E., Opgenoorth, H. J., Milan, S. E., Kauristie, K., et al. (2023). Signatures of wedgelets over Fennoscandia during the St Patrick's Day Storm 2015. *Journal of Space Weather and Space Climate*, *13*, 19. https://doi.org/10.1051/swsc/2023018

Schillings, A., Palin, L., Opgenoorth, H., Hamrin, M., Rosenqvist, L., Gjerloev, J., et al. (2022). Distribution and occurrence frequency of dB/dt spikes during magnetic storms 1980–2020. *Space Weather*, *20*(5), e2021SW002953. https://doi.org/10.1029/2021SW002953

Viljanen, A. (1997). The relation between geomagnetic variations and their time derivatives and implications for estimation of induction risks. *Geophysical Research Letters*, *24*(6), 631–634. https://doi.org/10.1029/97GL00538

Walach, M.-T., & Grocott, A. (2019). SuperDARN observations during geomagnetic storms, geomagnetically active times, and enhanced solar wind driving. *Journal of Geophysical Research: Space Physics*, *124*(7), 5828–5847. https://doi.org/10.1029/2019JA026816

Weigel, R., Klimas, A., & Vassiliadis, D. (2003). Solar wind coupling to and predictability of ground magnetic fields and their time derivatives. *Journal of Geophysical Research*, *108*(A7), 1298. https://doi.org/10.1029/2002JA009627

Weigel, R., Vassiliadis, D., & Klimas, A. (2002). Coupling of the solar wind to temporal fluctuations in ground magnetic fields. *Geophysical Research Letters*, *29*(19), 21-1–21-4. https://doi.org/10.1029/2002GL014740

Zou, Y., Dowell, C., Ferdousi, B., Lyons, L. R., & Liu, J. (2022). Auroral drivers of large dB/dt during geomagnetic storms. *Space Weather*, *20*(11), e2022SW003121. https://doi.org/10.1029/2022SW003121